J. Fluid Mech. (2015), *vol.* 779, *pp.* 325–350. © Cambridge University Press 2015
doi:10.1017/jfm.2015.420

Dimensionality, secondary flows and helicity in low-*Rm* MHD vortices

Nathaniel T. Baker[1,2,3,†], **Alban Pothérat**[1] **and Laurent Davoust**[2]

[1]Coventry University, Applied Mathematics Research Center, Priory Street, Coventry CV1 5FB, UK

[2]Grenoble-INP/CNRS/University Grenoble-Alpes, SIMaP, Electromagnetic Processing of Materials (EPM) Laboratory, F-38000 Grenoble, France

[3]CNRS LNCMI, 38042 Grenoble, France

(Received 25 March 2015; revised 8 June 2015; accepted 17 July 2015;
first published online 14 August 2015)

In this paper, we examine the dimensionality of a single electrically driven vortex bounded by two no-slip and perfectly insulating horizontal walls a distance h apart. The study was performed in the weakly inertial limit by means of an asymptotic expansion, which is valid for any Hartmann number. We show that the dimensionality of the leading order can be fully described using the single parameter l_z^v/h, where l_z^v represents the distance over which the Lorentz force is able to act before being balanced by viscous dissipation. The base flow happens to introduce inertial recirculations in the meridional plane at the first order, which are shown to follow two radically different mechanisms: inverse Ekman pumping driven by a vertical pressure gradient along the axis of the vortex, or direct Ekman pumping driven by a radial pressure gradient in the Hartmann boundary layers. We demonstrate that when the base flow is quasi-2D, the relative importance of direct and inverse pumping is solely determined by the aspect ratio η/h, where η refers to the width of the vortex. Of the two mechanisms, only inverse pumping appears to act as a significant source of helicity.

Key words: channel flow, MHD and electrohydrodynamics, vortex dynamics

1. Introduction

The question of the dimensionality of plane fluid layers is crucial to understanding the mechanisms of energy dissipation in turbulence, which occurs in a number of natural and industrial problems. Indeed, whether three-dimensionality is present or not decides whether turbulence transfers energy to large, weakly dissipative structures (two-dimensional turbulence) or efficiently dissipates energy at small scales in the bulk of the flow (Tabeling 2002; Clercx & Van Heijst 2009). These antagonistic behaviours may even co-exist in a number of real-world situations. For instance, planetary atmospheres feature quasi-two-dimensional (2D) large scales transporting small-scale three-dimensional (3D) turbulence (Lindborg 1999). Magnetohydrodynamic (MHD) turbulence in external magnetic fields (found in planetary cores or heat-extracting devices) also shares this feature (Klein & Pothérat 2010). Two-dimensionality can

† Email address for correspondence: nathaniel.baker@creta.cnrs.fr

be lost when either a third velocity component or velocity gradients appear across the fluid layer. Shats, Byrne & Xia (2010) showed that the former mechanism accompanied the disruption of the inverse cascade in two-dimensional turbulence. Transverse transport across the layer is all the more important as it is often associated with strong vorticity and therefore contributes to generating kinematic helicity (Deusebio & Lindborg 2014). This quantity not only alters the properties of turbulence but also greatly helps to sustain dynamos (Gilbert, Frisch & Pouquet 1988).

Thanks to the diverse ways that exist to two-dimensionalize a flow (e.g. shallow confinement, background magnetic field or rotation), a broad range of studies focusing on elementary structures have flourished only to reach the same conclusion: three-dimensionality occurs as a result of gradients across the fluid layer. From a practical point of view, such gradients are usually introduced by no-slip boundaries, which are an intrinsic feature of any real system. A first attempt to quantify the quasi-2D/3D structure of a single vortex confined in a shallow container was conducted by Satijn *et al.* (2001). They numerically studied the decay of a vortex, vertically bounded by a no-slip wall at the bottom and a free surface at the top, and showed that the relationship between shallow confinement and quasi-2D behaviour was not straightforward. Furthermore, they characterized the dimensionality of the vortex as a function of two non-dimensional parameters characterizing the diffusion of momentum in the vertical and horizontal directions respectively. Later on, Akkermans *et al.* (2008) were able to visualize the recirculations that take place in front of a dipolar vortex travelling in a similar configuration as above. Their main conclusion was that three-dimensionality resulted from vertical gradients of horizontal quantities (either velocity or forcing). It is only recently that the topological dimensionality of low-Rm MHD turbulence was elucidated by Pothérat & Klein (2014) in the light of diffusion lengths associated with the rotational part of the Lorentz force (first introduced by Sommeria & Moreau 1982). A recent study from Pothérat *et al.* (2013), based on numerical simulations and experimental observations, showed that meridional recirculations could follow either direct or inverse pumping.

There are, however, a number of limitations inherent to numerical and experimental methods that left the question in suspense since they could not investigate the finer properties of the flow. On the one hand, the main shortcoming of any numerical study comes from accessible computational power. Even though there was a recent breakthrough in solving low-Rm MHD turbulent flows in wall-bounded domains (Kornet & Pothérat 2015), the regimes reachable by direct numerical simulation (DNS) are, to date, still far from those encountered experimentally. On the other hand, experiments are limited by the resolution of the measuring devices in use. These issues prevent a thorough investigation of the boundary layers, which happen to be one of the most crucial sources of three-dimensionality.

The work that we present here takes place within the low-Rm MHD framework, in continuance of the studies described above. The goal of this paper is to characterize the relationship between the topological dimensionality of a wall-bounded electrically driven vortex and the occurring secondary flows. In order to do so, we focus on a single axisymmetric vortex confined between two horizontal planes. An analytical solution to the problem is derived by means of an asymptotic expansion in the weakly inertial limit, which is carried out up to the first order. The investigation performed here is valid for any Hartmann number, which makes it possible to investigate the finer properties of the boundary layers without concessions.

The model's geometry and governing equations are presented in § 2, and the exact solutions at leading and first order are given in §§ 3 and 4 respectively. Section 5 is

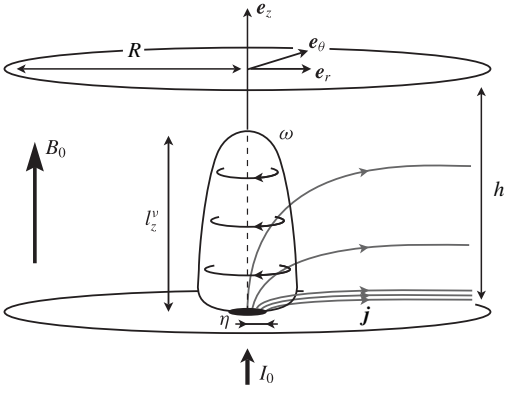

FIGURE 1. Sketch of the problem. An isolated vortex of height $l_z^v < h$ confined between two horizontal no-slip and electrically insulating walls a distance h apart.

dedicated to the validation of the method, while § 6 is dedicated to presenting and discussing our results.

2. Geometry and governing equations

Let us consider an axisymmetric flow taking place in a cylindrical cavity of radius R (see figure 1). As such, we focus exclusively on solutions that are invariant to rotations about the axis of the channel, i.e. $\partial_\theta = 0$. The domain is bounded by two no-slip horizontal walls located at $z = 0$ and $z = h$, and is filled with an electrically conducting fluid (typically a liquid metal such as Galinstan, of electrical conductivity $\sigma = 3.4 \times 10^6$ S m^{-1}, density $\rho = 6400$ kg m^{-3} and viscosity $\nu = 4 \times 10^{-7}$ m^2 s^{-1}). A static and uniform magnetic field $B_0\, \boldsymbol{e}_z$ is applied vertically. The low-Rm approximation is assumed to hold, meaning that the magnetic field induced by the flow is negligible compared to the imposed magnetic field (Roberts 1967). Consequently, the total magnetic field $\boldsymbol{B}$ is uniform across the domain and follows $\boldsymbol{B} = B_0\, \boldsymbol{e}_z$. In addition, the electric field $\boldsymbol{E}$ is derived from the electric potential ϕ according to $\boldsymbol{E} = -\nabla\phi$. A flow is driven by injecting electric current through an electrode of radius η located on the bottom plate. The top and bottom plates are perfectly electrically insulating otherwise, which forces the current to exit the channel through the sides. In anticipation of the upcoming calculations, the profile of injected current is assumed to be a smooth function, such as the Gaussian distribution:

$$j_z^w(r) = \frac{I_0}{\pi\eta^2} \exp\left[-(r/\eta)^2\right], \tag{2.1}$$

where I_0 is the total current injected inside the domain up to the correction factor $(1 - \exp[-(R/\eta)^2])$, which is almost identical to 1 for $R/\eta > 10$. Given this configuration, the electric current is known to flow radially, interacting with the vertical magnetic field to induce a patch of vertical vorticity right above the bottom Hartmann layer.

In the inertialess limit (Kalis & Kolesnikov 1980), the development of this patch of vorticity relies on the competition between two effects. On the one hand, the rotational part of the Lorentz force diffuses momentum along the magnetic field (Sommeria &

Moreau 1982), hence leading to a vortex extending in the z direction. On the other hand, viscous friction diffuses momentum isotropically, therefore opposing the growth of the vortex along z. Calling l_z^v the range of action of the Lorentz force, its diffusive effect takes place over the characteristic time $\tau_{2D} = (\rho/\sigma B_0^2)(l_z^v/\eta)^2$. Conversely, viscous dissipation takes place over the time $\tau_v = \eta^2/\nu$. Assuming a steady flow, the distance l_z^v over which the Lorentz force is able to act before being balanced by viscous dissipation is derived by equating the two effects, yielding:

$$\frac{l_z^v}{h} = \frac{\eta^2}{h^2} Ha, \tag{2.2}$$

where $Ha = B_0 h\sqrt{\sigma/\rho\nu}$ is the Hartmann number based on the height of the channel. Asymptotically speaking, $l_z^v/h \ll 1$ means that the diffusive effect of the Lorentz force is balanced by viscous dissipation long before momentum can reach the top wall. In this case, the distance l_z^v may be physically interpreted as the height of the vortex. In contrast, $l_z^v/h \gg 1$ means that momentum can be diffused far beyond the top wall. This process, however, is blocked by the presence of the no-slip top wall, which prevents the vortex from extending past it. The ratio l_z^v/h has been identified by Pothérat & Klein (2014) as the non-dimensional parameter defining whether the structure is able to feel the presence of the top wall, hence controlling its dimensionality: 3D when $l_z^v/h \ll 1$ and quasi-2D when $l_z^v/h \gg 1$.

From now on, let us use the dimensionless coordinates $\tilde{r} = r/\eta$ and $\tilde{z} = z/h$, as well as the non-dimensional variables $\tilde{u} = u/U$, $\tilde{\omega} = \omega\eta/U$, $\tilde{j} = j/\sigma U B_0$ and $\tilde{\phi} = \phi/UB_0\eta$. We also introduce the non-dimensional operator $\tilde{\boldsymbol{\nabla}}$ defined as

$$\tilde{\boldsymbol{\nabla}} = \left(\frac{\partial}{\partial\tilde{r}}, \frac{1}{\tilde{r}}\frac{\partial}{\partial\theta}, \frac{\eta}{h}\frac{\partial}{\partial\tilde{z}}\right). \tag{2.3}$$

The scaling for the velocity U is derived from the linear theory of quasi-2D electrically driven vortices put forward by Sommeria (1988). It is estimated from $U = (\Gamma/\eta)\sqrt{l_z^v/h}$, where $\Gamma = I_0/2\pi\sqrt{\sigma\rho\nu}$ is the circulation induced right above a point-like electrode through which flows the current I_0, when viscous friction in the horizontal plane is neglected. This scaling for U is representative of the velocity at the edge of the vortex core, whose radius results from the competition between the Lorentz force and viscous dissipation. Hence the explicit dependence of U on the ratio l_z^v/h. The governing equations consist of the steady-state vorticity equation for $\tilde{\boldsymbol{\omega}} = \tilde{\boldsymbol{\nabla}} \times \tilde{\boldsymbol{u}}$,

$$\frac{1}{N}\left(\tilde{\boldsymbol{u}}\cdot\tilde{\boldsymbol{\nabla}}\tilde{\boldsymbol{\omega}} - \tilde{\boldsymbol{\omega}}\cdot\tilde{\boldsymbol{\nabla}}\tilde{\boldsymbol{u}}\right) = \frac{1}{Ha}\left(\frac{l_z^v}{h}\right)^{-1}\tilde{\Delta}\tilde{\boldsymbol{\omega}} + \frac{1}{\sqrt{Ha}}\left(\frac{l_z^v}{h}\right)^{1/2}\frac{\partial\tilde{\boldsymbol{j}}}{\partial\tilde{z}}, \tag{2.4}$$

Ohm's law

$$\tilde{\boldsymbol{j}} = -\tilde{\boldsymbol{\nabla}}\tilde{\phi} + \tilde{\boldsymbol{u}} \times \boldsymbol{e}_z, \tag{2.5}$$

the conservation of mass

$$\tilde{\boldsymbol{\nabla}}\cdot\tilde{\boldsymbol{u}} = 0 \tag{2.6}$$

and charge

$$\tilde{\boldsymbol{\nabla}}\cdot\tilde{\boldsymbol{j}} = 0. \tag{2.7}$$

The problem at hand is governed by three non-dimensional parameters, namely the interaction parameter N based on the width of the injection electrode η, the Hartmann number Ha based on the height of the channel h and the ratio l_z^v/h:

$$N = \frac{\sigma B_0^2 \eta}{\rho U}, \quad Ha = B_0 h \sqrt{\frac{\sigma}{\rho \nu}}, \quad \frac{l_z^v}{h} = \frac{\eta^2}{h^2} Ha. \tag{2.8a–c}$$

The boundary conditions on the horizontal walls consist of no-slip boundaries

$$\tilde{\boldsymbol{u}}(\tilde{r}, 0) = \tilde{\boldsymbol{u}}(\tilde{r}, 1) = 0, \tag{i}$$

an imposed vertical current at the bottom wall

$$\tilde{j}_{\tilde{z}}(\tilde{r}, 0) = \tilde{j}_{\tilde{z}}^{w}(\tilde{r}) \tag{ii}$$

and a perfectly electrically insulating top wall

$$\tilde{j}_{\tilde{z}}(\tilde{r}, 1) = 0. \tag{iii}$$

In addition, we impose a perfectly conducting and free-slip radial boundary

$$\tilde{j}_{\tilde{z}}(\tilde{R}, \tilde{z}) = 0 \tag{iv}$$

and

$$\tilde{\boldsymbol{\tau}}_{\tilde{r}}(\tilde{R}, \tilde{z}) = 0, \tag{v}$$

where $\tilde{\boldsymbol{\tau}}_{\tilde{r}}$ represents the shear stress exerted on the wall whose normal vector is $\boldsymbol{e}_r$. These boundary conditions were chosen to match as closely as possible the experimental set-ups of Sommeria (1988) and Pothérat & Klein (2014), where a flow is driven by injecting a known amount of electric current I_0. The free-slip and perfectly conducting radial boundary can be physically interpreted as a pseudo-wall made of liquid metal, and was preferred over a no-slip boundary condition as it does not introduce parallel layers along the radial boundary. Keeping the experimental analogy in mind, the model we propose here focuses on an elementary structure, which has been extracted from an array of vortices.

Considering the scaling that was chosen for U, the normalized bottom boundary condition on the current $\tilde{j}_z^w$ is expressed as

$$\tilde{j}_{\tilde{z}}^{w}(\tilde{r}) = \frac{2}{\sqrt{Ha}} \left(\frac{l_z^v}{h}\right)^{-1} \exp\left(-\tilde{r}^2\right). \tag{2.9}$$

In other words, for a given value of Ha and l_z^v/h, the intensity of the total injected current is adjusted so that the intensity of the resulting flow remains comparable throughout all cases investigated.

We shall now consider a weakly inertial flow in the limit $N \gg 1$, and expand (2.4)–(2.7) using the regular perturbation series:

$$\tilde{\boldsymbol{j}} = \tilde{\boldsymbol{j}}^0 + N^{-1}\tilde{\boldsymbol{j}}^1 + N^{-2}\tilde{\boldsymbol{j}}^2 + O(N^{-3}), \tag{2.10}$$

$$\tilde{\boldsymbol{u}} = \tilde{\boldsymbol{u}}^0 + N^{-1}\tilde{\boldsymbol{u}}^1 + N^{-2}\tilde{\boldsymbol{u}}^2 + O(N^{-3}), \tag{2.11}$$

$$\tilde{\boldsymbol{\omega}} = \tilde{\boldsymbol{\omega}}^0 + N^{-1}\tilde{\boldsymbol{\omega}}^1 + N^{-2}\tilde{\boldsymbol{\omega}}^2 + O(N^{-3}). \tag{2.12}$$

3. Inertialess base flow

The equations governing the problem at leading order are

$$\tilde{\Delta}\tilde{\boldsymbol{\omega}}^0 = -\sqrt{Ha}\left(\frac{l_z^v}{h}\right)^{3/2}\frac{\partial \tilde{\boldsymbol{j}}^0}{\partial \tilde{z}}, \tag{3.1}$$

$$\tilde{\boldsymbol{j}}^0 = -\tilde{\boldsymbol{\nabla}}\tilde{\phi}^0 + \tilde{\boldsymbol{u}}^0 \times \boldsymbol{e}_z, \tag{3.2}$$

$$\tilde{\boldsymbol{\nabla}} \cdot \tilde{\boldsymbol{u}}^0 = 0, \tag{3.3}$$

$$\tilde{\boldsymbol{\nabla}} \cdot \tilde{\boldsymbol{j}}^0 = 0. \tag{3.4}$$

Solving $\tilde{\boldsymbol{\omega}}^0$ and $\tilde{\boldsymbol{j}}^0$ can be done separately by taking the Laplacian of the vorticity equation (2.4) on the one hand, and taking the Laplacian of twice the curl of Ohm's law (2.5) on the other hand. Combining them yields the following set of equations:

$$\tilde{\Delta}^2\tilde{\boldsymbol{\omega}}^0 = \left(\frac{l_z^v}{h}\right)^2\frac{\partial^2\tilde{\boldsymbol{\omega}}^0}{\partial \tilde{z}^2} \tag{3.5}$$

and

$$\tilde{\Delta}^2\tilde{\boldsymbol{j}}^0 = \left(\frac{l_z^v}{h}\right)^2\frac{\partial^2\tilde{\boldsymbol{j}}^0}{\partial \tilde{z}^2}. \tag{3.6}$$

It is quite remarkable that (3.5) and (3.6) can be solved independently, and depend on the same and unique parameter l_z^v/h. They remain nonetheless coupled via twice the curl of Ohm's law:

$$\tilde{\Delta}\tilde{\boldsymbol{j}}^0 = -\frac{1}{\sqrt{Ha}}\left(\frac{l_z^v}{h}\right)^{1/2}\frac{\partial \tilde{\boldsymbol{\omega}}^0}{\partial \tilde{z}}. \tag{3.7}$$

Equations (3.5) and (3.6) admit a purely azimuthal solution for $\tilde{\boldsymbol{u}}^0$ and a purely meridional solution for $\boldsymbol{j}^0$. Consequently, knowing either component $\tilde{\omega}_z^0$ or $\tilde{\omega}_r^0$, and $\tilde{j}_r^0$ or $\tilde{j}_z^0$ is enough to completely derive the solution at leading order. The boundary conditions associated with the leading order read

$$\tilde{\omega}_z^0(\tilde{r}, 0) = \tilde{\omega}_z^0(\tilde{r}, 1) = 0, \tag{i^0}$$

$$\tilde{j}_z^0(\tilde{r}, 0) = \tilde{j}_z^w(\tilde{r}), \tag{ii^0}$$

$$\tilde{j}_z^0(\tilde{r}, 1) = 0, \tag{iii^0}$$

$$\tilde{j}_z^0(\tilde{R}, \tilde{z}) = 0. \tag{iv^0}$$

In addition, we shall approximate boundary condition (v) by

$$\tilde{\omega}_z^0(\tilde{R}, \tilde{z}) = 0. \tag{v^0}$$

Boundary condition (v^0) is not entirely equivalent to the free-slip boundary condition (v), which can be rewritten in terms of $\tilde{\omega}_z^0$ as

$$\tilde{\omega}_z^0(\tilde{R}, \tilde{z}) = \frac{2}{\tilde{R}}\,\tilde{u}_\theta^0(\tilde{R}, \tilde{z}). \tag{3.8}$$

It is only in the limit $\tilde{R} \gg 1$ (since $\tilde{u}_\theta^0$ is of order 1) that boundary condition (v) may be approximated by (v^0). However, (v^0) offers a much simpler numerical implementation. Indeed, not only does it remove any remaining dependency on $\tilde{u}_\theta^0$, it also naturally introduces an orthogonal basis of functions on which the solution can be projected. From a practical point of view, we ensured that the edge of the channel was sufficiently far from the injection area in order to minimize the impact of this approximation on the flow (see § 5).

Solutions with separated variables of (3.5) and (3.6), which satisfy the coupling (3.7), as well as boundary conditions (iv^0) and (v^0) are of the form

$$\tilde{\omega}_{\tilde{z}}^0 = \sum_{n=1}^{\infty} \mathrm{J}_0(\lambda_n \tilde{r}) \sum_{i=1}^{4} A_{ni} \exp(s_{ni} \tilde{z}) \tag{3.9}$$

and

$$\tilde{j}_{\tilde{z}}^0 = \sum_{n=1}^{\infty} \mathrm{J}_0(\lambda_n \tilde{r}) \sum_{i=1}^{4} B_{ni} \exp(s_{ni} \tilde{z}), \tag{3.10}$$

where $\mathrm{J}_0(\tilde{r})$ refers to the zeroth-order Bessel function of first kind, and λ_n represents its nth root normalized by $\tilde{R}$. Note that solutions with separated variables that satisfy the coupling (3.7) and boundary condition (v^0) alone automatically satisfy boundary condition (iv^0), making the latter redundant and therefore unnecessary to close the problem. Conversely, a different set of boundary conditions at $\tilde{r} = \tilde{R}$ may not admit a solution with separated variables. The arguments for the exponentials s_{ni} may be expressed in terms of Ha and l_z^ν/h exclusively. They take four different values $s_{ni} = \pm s_{n\pm}$, where $s_{n\pm}$ is defined by

$$s_{n\pm} = \frac{Ha}{2} \left[1 \pm \sqrt{1 + \frac{4\lambda_n^2}{Ha} \left(\frac{l_z^\nu}{h} \right)^{-1}} \right]. \tag{3.11}$$

Restricting ourselves to cases that are relevant to MHD (i.e. cases where Ha is sufficiently large), the parameter $Ha^{-1}(l_z^\nu/h)^{-1}$ is expected to be much less than 1. Under this assumption, the roots $s_{n\pm}$ are expected to scale as

$$s_{n+} \sim \frac{h}{\delta} \quad \text{and} \quad s_{n-} \sim \lambda_n^2 \frac{h}{l_z^\nu}, \tag{3.12a,b}$$

where $\delta = h/Ha$ represents the thickness of the Hartmann boundary layer. That is to say, s_{n+} scales as $1/\delta$, and thus describes the boundary layers, while s_{n-} scales as λ_n^2/l_z^ν, which is the diffusion length associated with Bessel mode n. In this sense it represents the dimensionality of the bulk of the flow. From (3.7), coefficients A_{ni} and B_{ni} must satisfy

$$B_{ni} = -A_{ni} \frac{s_{ni}}{{s_{ni}}^2 \kappa - {\lambda_n}^2/\kappa}, \tag{3.13}$$

with $\kappa = Ha^{-1/2}(l_z^\nu/h)^{1/2}$. The coefficients A_{ni} are determined by solving the linear system stemming from the boundary conditions:

$$\left.\begin{aligned} \sum_{i=1}^{4} A_{ni} &= 0, \\ \sum_{i=1}^{4} A_{ni}\ \exp(s_{ni}) &= 0, \\ \sum_{i=1}^{4} A_{ni}\ \frac{s_{ni}}{{s_{ni}}^2\kappa - {\lambda_n}^2/\kappa} &= -\alpha_n, \\ \sum_{i=1}^{4} A_{ni}\ \frac{s_{ni}}{{s_{ni}}^2\kappa - {\lambda_n}^2/\kappa}\ \exp(s_{ni}) &= 0, \end{aligned}\right\} \qquad (\mathrm{S}^0)$$

where α_n results from the projection of $\tilde{j}_{\tilde{z}}^{w}(\tilde{r})$ on the basis of Bessel functions:

$$\alpha_n = \frac{2/\tilde{R}^2}{\mathrm{J}_1^2(\lambda_n \tilde{R})} \int_0^{\tilde{R}} \xi\, \tilde{j}_{\tilde{z}}^{w}(\xi)\, \mathrm{J}_0(\lambda_n \xi)\, \mathrm{d}\xi. \qquad (3.14)$$

At this stage, the supplementary radial components $\tilde{\omega}_{\tilde{r}}^0$ and $\tilde{j}_{\tilde{r}}^0$, as well as the velocity field $\tilde{\boldsymbol{u}}^0 = \tilde{u}_\theta^0\, \boldsymbol{e}_\theta$, can be readily determined by integrating $\tilde{\boldsymbol{\nabla}} \cdot \tilde{\boldsymbol{\omega}}^0 = 0$, $\tilde{\boldsymbol{\nabla}} \cdot \tilde{\boldsymbol{j}}^0 = 0$, and $\tilde{\boldsymbol{\omega}}^0 = \tilde{\boldsymbol{\nabla}} \times \tilde{\boldsymbol{u}}^0$ respectively.

4. Correction due to inertia

The equations governing the problem at first order are

$$\tilde{\boldsymbol{u}}^0 \cdot \tilde{\boldsymbol{\nabla}}\tilde{\boldsymbol{\omega}}^0 - \tilde{\boldsymbol{\omega}}^0 \cdot \tilde{\boldsymbol{\nabla}}\tilde{\boldsymbol{u}}^0 = \frac{1}{Ha}\left(\frac{l_z^\nu}{h}\right)^{-1} \tilde{\Delta}\tilde{\boldsymbol{\omega}}^1 + \frac{1}{\sqrt{Ha}}\left(\frac{l_z^\nu}{h}\right)^{1/2} \frac{\partial \tilde{\boldsymbol{j}}^1}{\partial \tilde{z}}, \qquad (4.1)$$

$$\tilde{\boldsymbol{j}}^1 = -\tilde{\boldsymbol{\nabla}}\tilde{\phi}^1 + \tilde{\boldsymbol{u}}^1 \times \boldsymbol{e}_z, \qquad (4.2)$$

$$\tilde{\boldsymbol{\nabla}} \cdot \tilde{\boldsymbol{u}}^1 = 0, \qquad (4.3)$$

$$\tilde{\boldsymbol{\nabla}} \cdot \tilde{\boldsymbol{j}}^1 = 0. \qquad (4.4)$$

Unlike the leading order (which is forced electrically at the bottom wall), the first order is driven by an azimuthal inertial force stemming from the base flow. In other words, $\tilde{\omega}_{\tilde{z}}^1$ and $\tilde{j}_{\tilde{z}}^1$ must satisfy homogeneous boundary conditions all along the edges of the domain. As a consequence, $\tilde{\omega}_{\tilde{z}}^1$ is strictly null and $\tilde{\phi}^1$ is uniform across the channel. In order to have a non-divergent solution on the axis of the channel, $\tilde{\omega}_{\tilde{r}}^1$ must also be null throughout the domain, meaning that the inertial correction to the base flow occurs in the meridional plane exclusively. In addition, the electric current becomes purely electromotive, since it is proportional to the velocity via Ohm's law. These arguments simplify the problem greatly by removing all couplings between mechanical and electrical quantities at first order. In the end, the equations reduce to

$$\tilde{F}_\theta^0\, \boldsymbol{e}_\theta = \frac{1}{Ha}\left(\frac{l_z^\nu}{h}\right)^{-1} \tilde{\Delta}\tilde{\boldsymbol{\omega}}^1 - \frac{1}{\sqrt{Ha}}\left(\frac{l_z^\nu}{h}\right)^{1/2} \frac{\partial \tilde{u}_{\tilde{r}}^1}{\partial \tilde{z}}\, \boldsymbol{e}_\theta, \qquad (4.5)$$

where $\tilde{F}_\theta^0$ is the inertial forcing originating from the nonlinear terms of the base flow:

$$\tilde{F}_\theta^0 = 2\,\frac{\tilde{u}_\theta^0\,\tilde{\omega}_r^0}{\tilde{r}}. \tag{4.6}$$

Owing to the previous arguments, (4.5) is non-trivial only in the $\boldsymbol{e}_\theta$ direction. It is solved by introducing the stream function $\tilde{\psi}^1 = \psi^1/U\eta$ such that $\tilde{\boldsymbol{u}}^1 = \tilde{\boldsymbol{\nabla}} \times (\tilde{\psi}^1\,\boldsymbol{e}_\theta)$ and $\tilde{\boldsymbol{\omega}}^1 = \tilde{\boldsymbol{\nabla}} \times \tilde{\boldsymbol{\nabla}} \times (\tilde{\psi}^1\,\boldsymbol{e}_\theta)$, yielding the following equation for $\tilde{\psi}^1$:

$$\frac{l_z^\nu}{h}\,Ha\,\tilde{F}_\theta^0 = -\left[\tilde{\Delta} - \frac{1}{\tilde{r}^2}\right]^2 \tilde{\psi}^1 + \left(\frac{l_z^\nu}{h}\right)^2 \frac{\partial^2 \tilde{\psi}^1}{\partial \tilde{z}^2}, \tag{4.7}$$

where $\tilde{\Delta}$ represents the scalar Laplace operator in cylindrical coordinates. Again, the intensity of the flow depends on the interaction parameter N, while the topology of the first-order recirculations depends on Ha and the ratio l_z^ν/h. Since mechanical and electrical quantities are decoupled at first order, the boundary conditions associated with this problem boil down to no-slip and non-penetrating boundaries at the top and bottom walls, and no shear stress at the radial boundary:

$$\left.\frac{\partial \tilde{\psi}^1}{\partial \tilde{z}}\right|_{\tilde{r},0} = \left.\frac{\partial(\tilde{r}\tilde{\psi}^1)}{\partial \tilde{r}}\right|_{\tilde{r},0} = 0, \tag{i_0^1}$$

$$\left.\frac{\partial \tilde{\psi}^1}{\partial \tilde{z}}\right|_{\tilde{r},1} = \left.\frac{\partial(\tilde{r}\tilde{\psi}^1)}{\partial \tilde{r}}\right|_{\tilde{r},1} = 0, \tag{i_1^1}$$

$$\frac{\partial}{\partial \tilde{r}}\left(\frac{1}{\tilde{r}}\,\frac{\partial(\tilde{r}\tilde{\psi}^1)}{\partial \tilde{r}}\right)\bigg|_{\tilde{R},\tilde{z}} - \left.\frac{\partial^2 \tilde{\psi}^1}{\partial \tilde{z}^2}\right|_{\tilde{R},\tilde{z}} = 0. \tag{v^1}$$

Solutions of (4.7) are sought as the sum of a homogeneous solution $\tilde{\psi}_h^1(\tilde{r},\tilde{z})$ and a particular solution of the problem with inertial forcing $\tilde{\psi}_f^1(\tilde{r},\tilde{z})$. The homogeneous problem is very similar to the one solved earlier and reads

$$\tilde{\psi}_h^1(\tilde{r},\tilde{z}) = \sum_{n=1}^{\infty} \mathrm{J}_1(\mu_n\,\tilde{r}) \sum_{i=1}^{4} C_{ni}\,\exp(p_{ni}\,\tilde{z}), \tag{4.8}$$

where $\mathrm{J}_1(\tilde{r})$ is the first-order Bessel function of the first kind and μ_n represents its nth root normalized by $\tilde{R}$. As for the leading order, the roots p_{ni} are defined as

$$p_{n\pm} = \frac{Ha}{2}\left[1 \pm \sqrt{1 + \frac{4\mu_n^2}{Ha}\left(\frac{l_z^\nu}{h}\right)^{-1}}\right]. \tag{4.9}$$

The particular solution ψ_f^1 is found by expanding $\tilde{F}_\theta^0$ as a Fourier–Bessel series of $\mathrm{J}_1(\mu_n\,\tilde{r})$:

$$\tilde{F}_\theta^0(\tilde{r},\tilde{z}) = \sum_{n=1}^{\infty} \mathrm{J}_1(\mu_n\,\tilde{r})\;\varphi_n(\tilde{z}), \tag{4.10}$$

with

$$\varphi_n(\tilde{z}) = -2\,\kappa \sum_{i,j=1}^{\infty} \sum_{k,l=1}^{4} \beta_{nij}\, \frac{A_{ik}\, A_{jl}\, s_{jl}}{\lambda_i\, \lambda_j}\ \exp[(s_{ik} + s_{jl})\,\tilde{z}], \tag{4.11}$$

where

$$\beta_{nij} = \frac{2/\tilde{R}^2}{J_2^2(\mu_n\,\tilde{R})} \int_0^{\tilde{R}} \xi\, \mathrm{J}_1(\lambda_i\,\xi)\, \mathrm{J}_1(\lambda_j\,\xi)\, \mathrm{J}_1(\mu_n\,\xi)\, \mathrm{d}\xi. \tag{4.12}$$

The response of the flow to the forcing is therefore

$$\tilde{\psi}_f^1(\tilde{r}, \tilde{z}) = \sum_{n=1}^{\infty} \mathrm{J}_1(\mu_n\,\tilde{r}) \sum_{i,j,k,l} K_{nijkl} \exp[(s_{ik} + s_{jl})\,\tilde{z}], \tag{4.13}$$

where

$$K_{nijkl} = \frac{2\dfrac{\beta_{nij}}{\kappa} \left(\dfrac{l_z^v}{h}\right)^2 \dfrac{A_{ik}\, A_{jl}\, s_{jl}}{\lambda_i\, \lambda_j}}{\mu_n^4 - \left[\left(\dfrac{l_z^v}{h}\right)^2 + 2(\mu_n\,\kappa)^2\right](s_{ik} + s_{jl})^2 + [\kappa\,(s_{ik} + s_{jl})]^4}. \tag{4.14}$$

Note that at this stage the value of K_{nijkl} is fully determined, since it depends only on quantities resulting from the base flow. Finally,

$$\tilde{\psi}^1 = \sum_{n=1}^{\infty} \mathrm{J}_1(\mu_n\,\tilde{r}) \left(\sum_{i=1}^{4} C_{ni}\ \exp(p_{ni}\,\tilde{z}) + \sum_{i,j,k,l} K_{nijkl} \exp[(s_{ik} + s_{jl})\tilde{z}] \right), \tag{4.15}$$

where the integration constants C_{ni} are determined from the boundary conditions:

$$\left.\begin{aligned} \sum_{i=1}^{4} C_{ni} &= -\sum_{i,j,k,l} K_{nijkl}, \\ \sum_{i=1}^{4} C_{ni}\, p_{ni} &= -\sum_{i,j,k,l} K_{nijkl}(s_{ik} + s_{jl}), \\ \sum_{i=1}^{4} C_{ni} \exp(p_{ni}) &= -\sum_{i,j,k,l} K_{nijkl} \exp(s_{ik} + s_{jl}), \\ \sum_{i=1}^{4} C_{ni}\, p_{ni} \exp(p_{ni}) &= -\sum_{i,j,k,l} K_{nijkl}(s_{ik} + s_{jl}) \exp(s_{ik} + s_{jl}). \end{aligned}\right\} \tag{S^1}$$

To summarize, (3.9), (3.10) and (4.15) provide a complete solution for the flow at order $O(N^{-1})$ in the limit $N \gg 1$, and for any arbitrary value of Ha or l_z^v/h. This solution is shown to be exclusively governed by three non-dimensional parameters: N, which determines the intensity of the flow (as in the theory of Pothérat, Sommeria & Moreau 2000); Ha, which controls the thickness of the boundary layers (as in the classical theory); and l_z^v/h, which defines the dimensionality of the flow. With such a formulation of the problem, one can clearly see that the geometrical aspect ratio η/h is not the most appropriate parameter to precisely describe the dimensionality of the

base flow. However, l_z^v/h is. This may explain why the height-to-width aspect ratio of the vortex can be seen as a 'confusing parameter' (Satijn *et al.* 2001). It is also worth noting that the even orders correspond to the azimuthal component of the flow, while the odd orders give corrections in the meridional plane. This behaviour was also found in the analogous configuration described by Davoust, Achard & Drazek (2015), which consists of an annular channel with a rotating bottom. We shall now numerically evaluate this solution to find how the topological dimensionality of the base flow impacts the secondary recirculations.

5. Numerical methods

5.1. *Algorithm description*

An in-house FORTRAN95 code was developed to evaluate numerically $\tilde{\omega}_{\tilde{z}}^0(\tilde{r}, \tilde{z})$, $\tilde{j}_{\tilde{z}}^0(\tilde{r}, \tilde{z})$ and $\tilde{\psi}^1(\tilde{r}, \tilde{z})$. The goal of the solver was to compute the Fourier–Bessel coefficients A_{ni} and C_{ni}. That is to say, solve systems (S^0) and (S^1) in order to reconstruct the solution via (3.9), (3.10) and (4.15) respectively. The FMLIB 1.3 multi-precision package (Smith 1991) was used to ensure sufficient accuracy of the solution for any value of Ha. The input parameters for our code were Ha, l_z^v/h and the number of modes N_{mode}. The structure of the algorithm is as follows.

(*a*) Set the working precision based on Ha.
(*b*) Generate the zeros of Bessel functions J_0 and J_1.
(*c*) Compute α_n and β_{nij} according to (3.14) and (4.12) respectively, by evaluating the integrals using a Gauss–Legendre quadrature rule of order 100.
(*d*) Compute $s_{n\pm}$ and $p_{n\pm}$ according to (3.11) and (4.9) respectively.
(*e*) Compute K_{nijkl} according to (4.14).
(*f*) Find A_{ni} and C_{ni} by solving (S^0) and (S^1) with a Gauss–Jordan elimination method.
(*g*) Discretize the domain, build the solution according to (3.9), (3.10) and (4.15), and convert the output to double precision.

5.2. *Convergence test*

In this section, we evaluate the number of terms necessary to accurately represent infinite sums. To this end, let us introduce ϵ^n, the relative error at order n respectively defined by

$$\epsilon^0(N_{mode}) = \frac{\|\tilde{u}_\theta^0(N_{mode}) - \tilde{u}_\theta^0(N_{max})\|_2}{\|\tilde{u}_\theta^0(N_{max})\|_2} \tag{5.1}$$

and

$$\epsilon^1(N_{mode}) = \frac{\|\tilde{\psi}^1(N_{mode}) - \tilde{\psi}^1(N_{max})\|_2}{\|\tilde{\psi}^1(N_{max})\|_2}, \tag{5.2}$$

where $\|\cdot\|_2$ represents the classically defined $\mathscr{L}^2$-norm. ϵ^n compares the difference between a run computed with the number of modes N_{mode} and the reference case computed with the highest number of modes N_{max}. For all cases, N_{max} was set to 80. The convergence tests were conducted for three different channel radii $\tilde{R} = 5$, 10 and 20, since this parameter was expected to impact the accuracy of the solution. According to figure 2, the number of modes required to achieve a given relative error unsurprisingly increases with $\tilde{R}$. Indeed, the vortex becomes thinner with respect to the

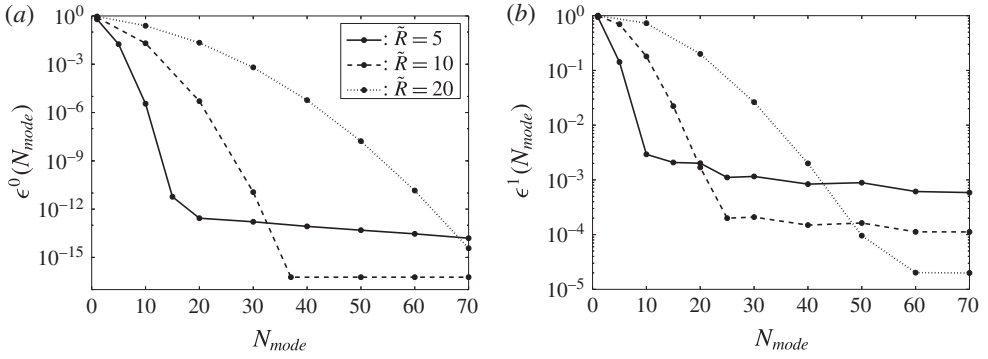

FIGURE 2. Convergence test. (*a*) Leading order, (*b*) first order. Legend in (*b*) same as for (*a*).

total width of the channel, meaning that modes of smaller wavelengths are required to capture it precisely.

At leading order, increasing the number of modes with $\tilde{R}=10$ and $\tilde{R}=20$ steadily improves the accuracy of the solution until ϵ^0 eventually reaches double precision. The behaviour of ϵ^0 for $\tilde{R}=5$ is completely different: fast convergence is observed at first, followed by a region where accuracy hardly improves with N_{mode}. This effect is first evidence that the radial wall is too intrusive for $\tilde{R}=5$.

At first-order, ϵ^1 follows a similar behaviour regardless of the position of the radial wall: increasing the number of modes improves the residual error before it levels off. This behaviour comes from the discrepancy that exists between the real inertial forcing F_θ^0 (which is only approximately null at the edge due to the simplified boundary condition) and its Fourier–Bessel expansion, which is strictly null by definition of $\mathrm{J}_1(\mu_n\tilde{R})$. This discrepancy introduces Gibbs phenomena close to the edge of the channel. It is, however, important to note that the oscillations are confined to a region close to the edge. Additionally, they become less and less an issue as R is increased, since F_θ^0 naturally vanishes away from the core of the vortex.

The conclusion of this convergence analysis is that $\tilde{R}$ must be as large as possible to prevent numerical artefacts. The operating point chosen was $\tilde{R}=20$ and $N_{mode}=50$, which gave us a good compromise between accuracy and computational time (proportional to N_{mode}^3). With these settings, the solution at leading order is reliable up to eight significant digits, and the relative accuracy of the first order is better than 0.01 %.

5.3. *Validity of the radial boundary condition*

Figure 3 shows the radial profiles of azimuthal velocity evaluated at the middle of the channel for different radial wall distances. In the case at hand, $l_z^v/h = 1000$, meaning that the base flow is already quasi-2D. According to figure 3, the azimuthal velocity follows a $1/\tilde{r}$ decay law outside the core of the vortex. This behaviour is in agreement with the quasi-2D theory developed by Sommeria (1988) for a vortex driven by injecting current through a point-like electrode. This suggests that the radial distribution of injected current plays a minor role in determining the actual shape of the vortex, and that a Gaussian distribution provides a very good representation of a thin current injection electrode (at least when the flow is quasi-2D). This point will be further studied in the following section.

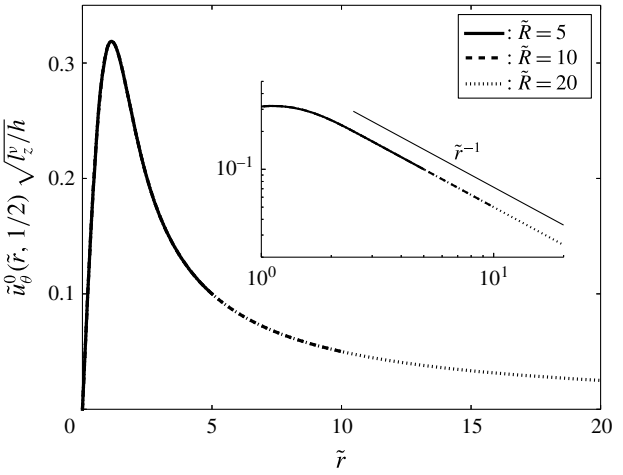

FIGURE 3. Velocity profile at the middle of the channel, obtained for $Ha=456$ and $l^v_z/h=1000$. The inset highlights how the azimuthal velocity decays as $1/\tilde{r}$ away from the core of the vortex.

	$\tilde{R}=5$	$\tilde{R}=10$	$\tilde{R}=20$
$\tilde{\tau}^0_{r\theta}$	3.99×10^{-2}	1.00×10^{-2}	2.50×10^{-3}

TABLE 1. Shear stress at the radial boundary.

Table 1 gives an estimation of the leading-order shear stress at the edge of the domain,

$$\tilde{\tau}^0_{r\theta}=\tilde{r}\,\frac{\partial}{\partial\tilde{r}}\left(\frac{\tilde{u}^0_\theta}{\tilde{r}}\right)\bigg|_{\tilde{R},\tilde{z}}, \tag{5.3}$$

for different positions of the radial wall. It gives an *a posteriori* confirmation that the simplified radial boundary condition (v^0) tends towards a free-slip boundary condition when $\tilde{R}$ is increased. Furthermore, we find that $\tilde{\tau}^0_{r\theta}$ scales as $1/\tilde{R}^2$ to a very good precision. This provides supplementary evidence that the solution is reliable, since $\tilde{u}^0_\theta(\tilde{R})$ is expected to scale as $1/\tilde{R}$ for quasi-2D structures. In 3D flows, $\tilde{u}^0_\theta(\tilde{R})$ is expected to be lower, and so should be $\tilde{\tau}^0_{r\theta}$. For $\tilde{R}=20$, the order of magnitude of the shear stress at the wall is 10^{-3}.

5.4. *Sensitivity to the injection profile and relevance to experiments*

Let us now investigate the sensitivity of the base flow to the bottom electric boundary condition. This question is all the more legitimate as the very existence of the flow relies on the injection of electric current at the bottom. The spatial distribution of current density can thus be expected to shape the resulting flow. In order to quantify the relevance of our model to describing electrically driven vortices, we shall compare the flow induced by two different injection profiles:

$$j^w_z(r)=\frac{I_0}{\pi\eta^2}\exp\left[-(r/\eta)^2\right] \tag{5.4}$$

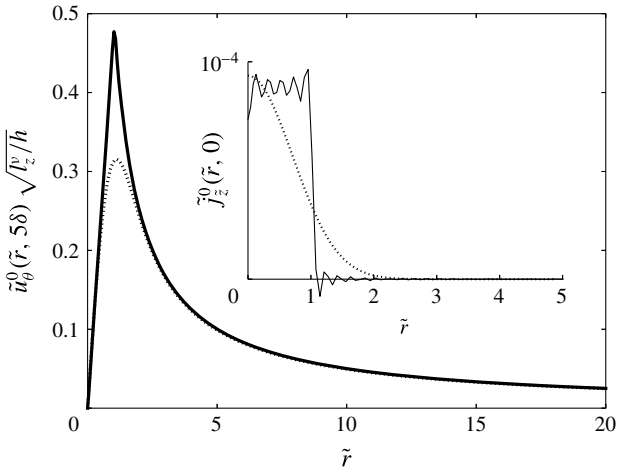

FIGURE 4. Velocity profile right above the Hartmann layer induced by two different radial distributions of electric current. ····: flow resulting from a Gaussian distribution of current. —: flow resulting from a step distribution of current. The inset shows the respective current profiles at the bottom wall $\tilde{j}_z^0(\tilde{r}, 0)$.

and

$$j_z^w(r) = \frac{I_0}{\pi\eta^2}[H(r) - H(r-\eta)], \tag{5.5}$$

where $H(r)$ refers to the Heaviside step function. These two particular profiles were chosen so that the typical width of the electrode remained η and the total amount of electric current injected in the domain was I_0. For both cases Ha and l_z^v/h were set to $Ha = 456$ and $l_z^v/h = 1000$. Furthermore, the number of modes used to expand the Gaussian distribution was $N_{mode} = 50$ (in agreement with § 5.2), while $N_{mode} = 200$ was imposed to expand the step distribution. A much higher number of modes is obviously necessary for the latter profile since it is singular at $\tilde{r} = 1$.

Figure 4 shows the leading order azimuthal velocity along $\tilde{r}$, right above the bottom Hartmann layer ($\tilde{z} = 5/Ha$) for both current distributions. The associated current profiles are displayed in the inset. The first striking feature of figure 4 is that both velocity profiles follow the same asymptotic behaviour whether close to the axis of the vortex or away from its core. This behaviour comes from the fact that the lateral diffusion of momentum is driven by viscous dissipation, and is therefore independent of the injected electric current. As already discussed in § 5.3, both vortices follow a $1/\tilde{r}$ decay law away from their core, which is expected for quasi-2D structures. The velocity peak is found at $\tilde{r} = 1$ in both cases, which corresponds to the outer edge of the electrode. The main difference between the two profiles, however, is the value of the peak, which is approximately twice as large for the step distribution. As a result, we can expect the Gaussian distribution to slightly underestimate the magnitude of the inertial terms. However, since the shape of the flow is identical in both cases, the mechanisms driving the first-order recirculations will be unchanged (recall that the inertial forcing stems from mechanical quantities only).

As in experiments on electrically driven flows, the intensity of the vortex is controlled by the total imposed current through the electrode (Sommeria 1988; Messadek & Moreau 2002; Klein & Pothérat 2010; Pothérat & Klein 2014).

Nevertheless, it is also possible to impose a fixed voltage between electrodes, or between the injection electrode and the side wall. Kalis & Kolesnikov (1980) showed that imposing a uniform current density or uniform voltage at the electrode was essentially equivalent as far as the topology of the base flow was concerned. We can therefore assert that our model is a faithful representation of electrically driven vortices in experiments, even if a Gaussian distribution of current is imposed at the bottom.

It is also worth noting that although high-frequency oscillations exist in the expansion of the step distribution (such oscillations are unavoidable regardless of the number of modes taken into account, as a result of its singular nature), they do not appear in the induced flow. This effect comes from the analytical approach that was used, and more specifically from the systematic use of dot products to build the solution. This provides supplementary evidence that our model is reliable and robust, since it is insensitive to numerical artefacts.

6. Results

Numerical experiments were conducted for four values of the Hartmann number: $Ha = 456$, 911, 1822 and 3644. For all values of Ha, the ratio l_z^v/h was set within the range 10^{-2} to 10^5. From now on, the low-Ha case refers to $Ha = 456$, while the high-Ha case refers to $Ha = 3644$.

6.1. *Inertialess base flow*

Figure 5 depicts the base flow for $Ha = 3644$, and for three values of l_z^v/h: 0.01, 1 and 10 000. The lower Ha cases are not presented here, since they look almost identical. As a matter of fact, the only difference between them at leading order is the thickness of the boundary layers.

The dimensionality of the flow can be estimated by comparing the intensity of the velocity field along the top and bottom walls. For $l_z^v/h = 0.01$, the flow is mostly concentrated at the bottom of the channel (i.e. where the electric forcing takes place), while there is absolutely no flow at the top. The base flow is said to be weakly 3D (in the sense of Klein & Pothérat 2010), meaning that although the topological patterns remain the same across the channel (that is to say, the vortex stays columnar), their intensity still depends on $\tilde{z}$. This behaviour is a consequence of the Lorentz force not being strong enough to compete with viscous dissipation beyond l_z^v, which is in this case a hundred times smaller than h. In other words, weak three-dimensionality characterizes a flow where two adjacently stacked layers of horizontal velocity experience differential rotation, as a result of vertical gradients. As l_z^v/h increases, the range of action of the Lorentz force becomes longer, and momentum is diffused further up the channel. For $l_z^v/h = 10\,000$, the flow is quasi-2D in the sense that all velocity gradients along $\tilde{z}$ have been smoothed out outside the boundary layers (a $\tilde{z}$-dependence always exists in the top and bottom Hartmann layers due to the no-slip walls). The vortex spans across the channel and is therefore able to feel the effect of the top wall.

Figure 5 also displays current densities. As expected, they are highest where strong velocity gradients exist, i.e. in the boundary layers and in the core of the vortex. For all cases, we have verified that, up to numerical precision, exactly half of the total current injected in the channel flows within the bottom Hartmann layer, while the other half flows vertically. This result confirms the heuristic prediction of Pothérat & Klein (2014). For low values of l_z^v/h (0.01 and 1), the velocity gradient along

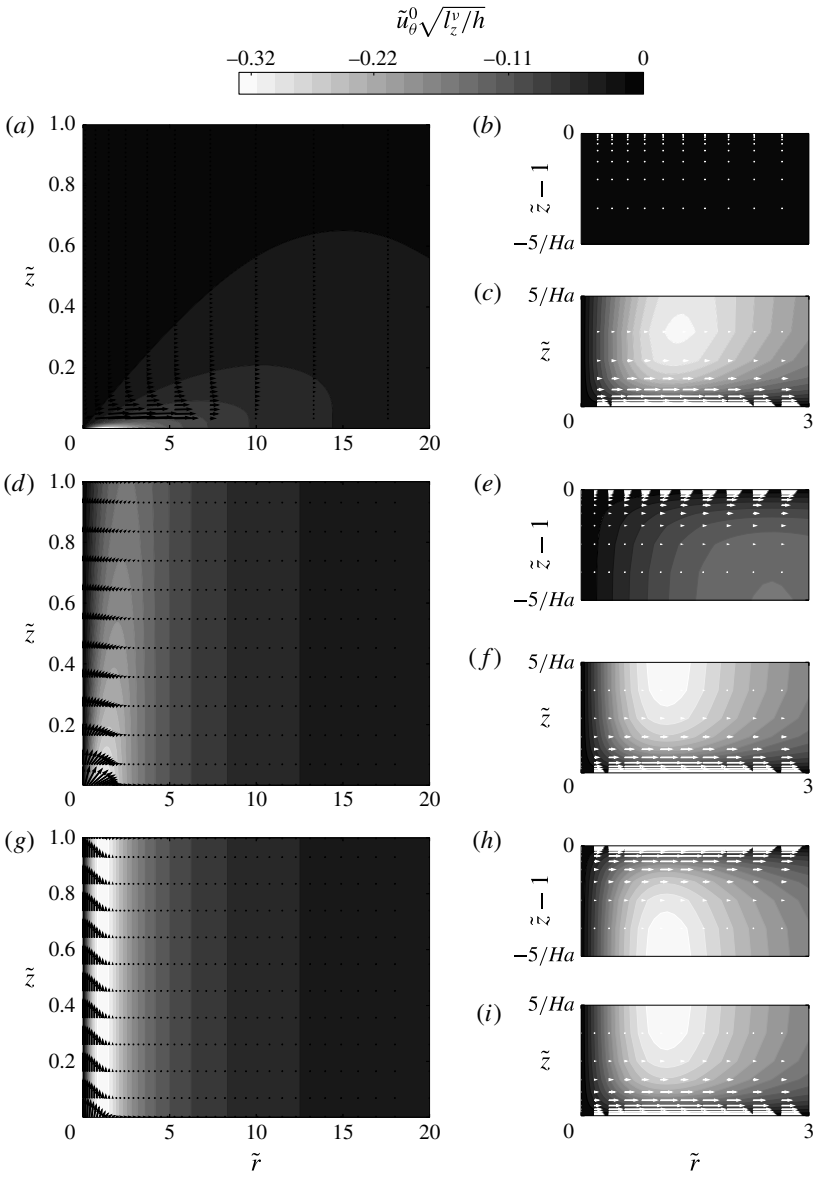

FIGURE 5. Solution at leading order for $Ha = 3644$, and for $l_z^v/h = 0.01$ (*a*), 1 (*d*) and 10 000 (*g*) respectively. The magnitude of $\tilde{u}_\theta^0\sqrt{l_z^v/h}$ is indicated by filled contours. The electric current density is represented by black and white vectors (colour choice is just a matter of contrast). Scaling of vectors has been adapted to compensate the much higher current densities in the boundary layers. Insets: close-up view of the top Hartmann layer (*b*,*e*,*h*) and bottom Hartmann layer (*c*,*f*,*i*) featuring the usual exponential profile for the electric current.

$\tilde{z}$ introduced by three-dimensionality progressively extracts the vertical current into the bulk, channelling it towards the edge of the domain. For $l_z^v/h = 10\,000$, however, quasi-two-dimensionality has smoothed out all velocity gradients along $\tilde{z}$ in the bulk:

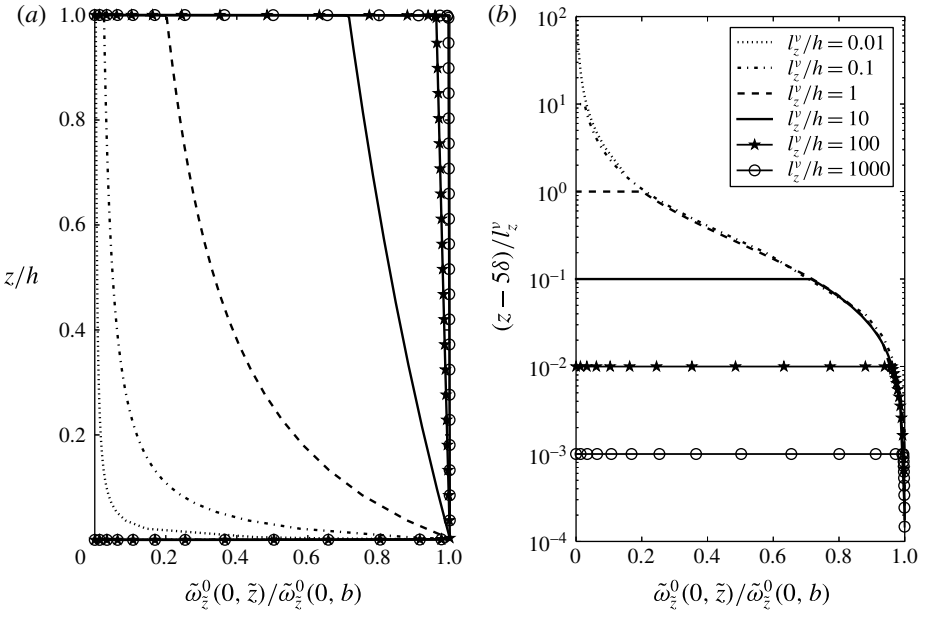

FIGURE 6. Axial vorticity $\tilde{\omega}_z^0(0,\tilde{z})$ normalized by the vorticity right outside the bottom Hartmann layer $\tilde{\omega}_z^0(0,b)$ for $Ha = 3644$. (*a*) z is normalized by the height of the channel h. (*b*) z is normalized by the Lorentz force diffusion length l_z^v.

the vertical current flows exclusively within the core of the vortex and the top and bottom Hartmann layers.

Close-up views of the Hartmann layers are given in the insets of figure 5. It is clear from these figures that the electric content of all bottom Hartmann layers is quite similar, but that the electric content of the top Hartmann layer depends on how far the Lorentz force is able to diffuse momentum along $\tilde{z}$. As expected, the electric current decreases away from the walls, following an exponential profile in all cases.

The dimensionality of the base flow is better quantified with figure 6. From now on, $\tilde{\omega}_z^0(\tilde{r},\, t)$ and $\tilde{\omega}_z^0(\tilde{r},\, b)$ refer to the vorticity right outside the top and bottom Hartmann layers respectively (see Pothérat, Sommeria & Moreau (2002) for a mathematically rigorous definition of this concept). Figure 6 portrays the profile of vertical vorticity $\tilde{\omega}_z^0(0,\tilde{z})$ normalized by $\tilde{\omega}_z^0(0,b)$ along the axis of the channel. In figure 6(*a*), all structures evolve in a channel of fixed height ($\tilde{z}$ is normalized by h). This representation highlights the effect of the ratio l_z^v/h on the dimensionality of the base flow: as l_z^v/h increases, the momentum induced right above the injection electrode is diffused farther and farther by the Lorentz force, hence progressively smoothing out velocity gradients along $\tilde{z}$. In figure 6(*b*), all curves are shifted down by 5δ to account for the varying thickness of the Hartmann layer, and then normalized by l_z^v. The collapse of all curves in these variables clearly indicates that all vortices follow a universal profile, which is solely defined by the competition between the Lorentz force and viscous dissipation. In other words, the effect of the vertical confinement is local, and only consists in ending the universal profile by introducing a no-slip boundary: the presence of the top wall is felt over a distance whose order of magnitude is no larger than the thickness of the Hartmann layer.

Figure 7 compares the vorticity on the axis of the channel right below the top Hartmann layer to the vorticity right above the bottom one. This figure highlights how

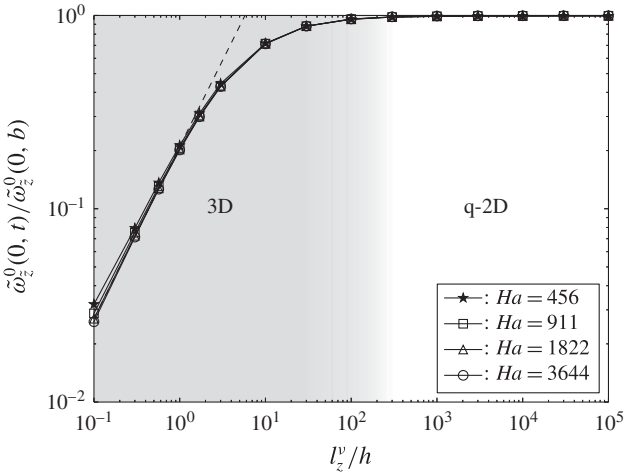

FIGURE 7. Dimensionality of the base flow: 3D when $\tilde{\omega}_z^0(0,t)/\tilde{\omega}_z^0(0,b) < 1$; quasi-2D when $\tilde{\omega}_z^0(0,t)/\tilde{\omega}_z^0(0,b) \to 1$. A colour gradient is used to highlight the smooth transition from a 3D to a quasi-2D base flow as the parameter l_z^v/h increases.

all the information about the dimensionality of the base flow is exclusively contained within the single parameter l_z^v/h, regardless of the value of the Hartmann number. Furthermore, the transition from 3D to quasi-2D base flows appears to be a gradual process that occurs around $l_z^v/h \sim 100$. This effect was also noted by Klein & Pothérat (2010) in turbulent flows.

6.2. *The topology of meridional recirculations*

Figures 8 and 9 give a complete view of the velocity field for the low- and high-Ha cases. When the base flow is 3D ($l_z^v/h < 100$), a large counter-clockwise recirculation dominates the flow. This phenomenon has been observed by Akkermans *et al.* (2008) in electrolytes, and by Pothérat *et al.* (2013) in steady and turbulent liquid metal flows. It is driven by an axial pressure gradient that builds up along the axis of the vortex as a result of the negative gradient of azimuthal velocity along $\boldsymbol{e}_z$. Since the associated flow recirculates in the opposite direction to Ekman pumping, and both are driven by differential rotation, it was called inverse Ekman pumping by the latter authors. As the base flow becomes increasingly quasi-2D ($l_z^v/h > 100$), a clockwise recirculation becomes visible at the bottom of the domain and grows steadily with l_z^v/h. The secondary flow is then composed of two counter-rotating structures, which correspond to direct Ekman pumping (Ekman 1905), or what is also called the 'tea-cup effect'. Unlike inverse pumping (which stems from a pressure gradient along the axis of the vortex), direct pumping is driven by a radial pressure gradient inside the boundary layers, which develops in the bulk to oppose centrifugal forces. To further elucidate the role of pressure gradients on the topology of secondary flows, let us reconstruct numerically from the Navier–Stokes equation projected along $\boldsymbol{e}_z$ the vertical pressure gradient along the axis of the vortex:

$$\frac{\partial \tilde{p}^0}{\partial \tilde{z}} = \frac{2}{Ha}\left(\frac{l_z^v}{h}\right)^{-1} \left.\frac{\partial^2 \tilde{u}_{\tilde{z}}^1}{\partial \tilde{r}^2}\right|_{0,\tilde{z}} + \frac{1}{Ha^2} \left.\frac{\partial^2 \tilde{u}_{\tilde{z}}^1}{\partial \tilde{z}^2}\right|_{0,\tilde{z}}. \tag{6.1}$$

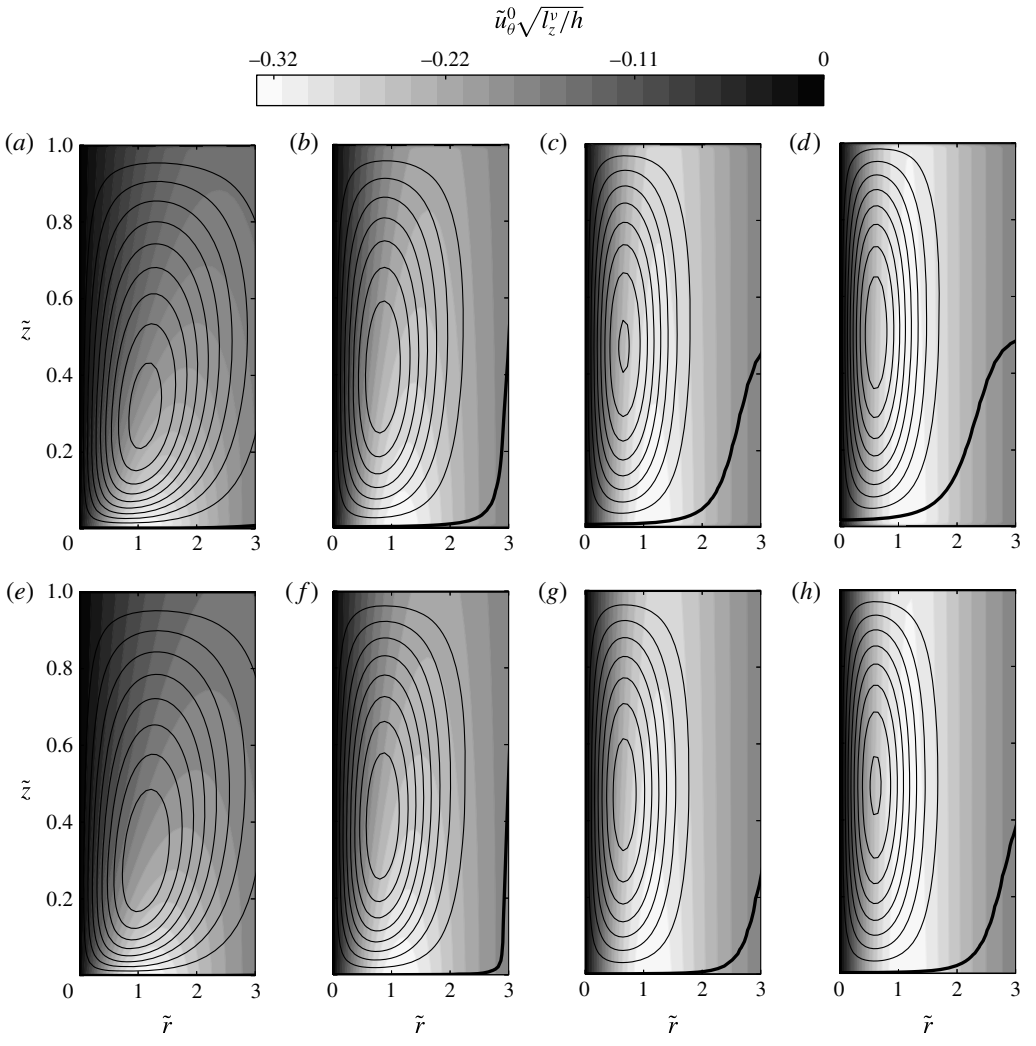

FIGURE 8. Complete velocity field for 3D base flows. (*a–d*) $Ha = 456$; (*e–h*) $Ha = 3644$. The magnitude of $\tilde{u}_\theta^0$ is indicated by filled contours. Streamlines correspond to iso-values of ψ^1. ——: counter-clockwise recirculation ($\psi^1 < 0$), ▬: $\psi^1 = 0$. (*a*,*e*) $l_z^v/h = 1$; (*b*,*f*) $= 3$; (*c*,*g*) $= 10$; (*d*,*h*) $= 30$.

The profiles of pressure gradient along the axis of the vortex are represented in figure 10 in order to illustrate the previous argument. When the flow is 3D, a positive pressure gradient exists in the bulk, whose effect is to drive a jet down along the axis of the vortex. Because this phenomenon is entirely governed by velocity gradients in the core, it is no surprise that the intensity of the inverse pumping is driven by l_z^v/h. As a result of quasi-two-dimensionality, the dependence of the pressure (or any other quantity for that matter) on $\tilde{z}$ in the bulk disappears. However, a very strong vertical pressure gradient exists at both ends of the axis as a result of a converging radial flow within the boundary layers.

Interestingly, a negative pressure gradient always exists in the bottom Hartmann layer regardless of whether the base flow is 3D or quasi-2D. This means that a

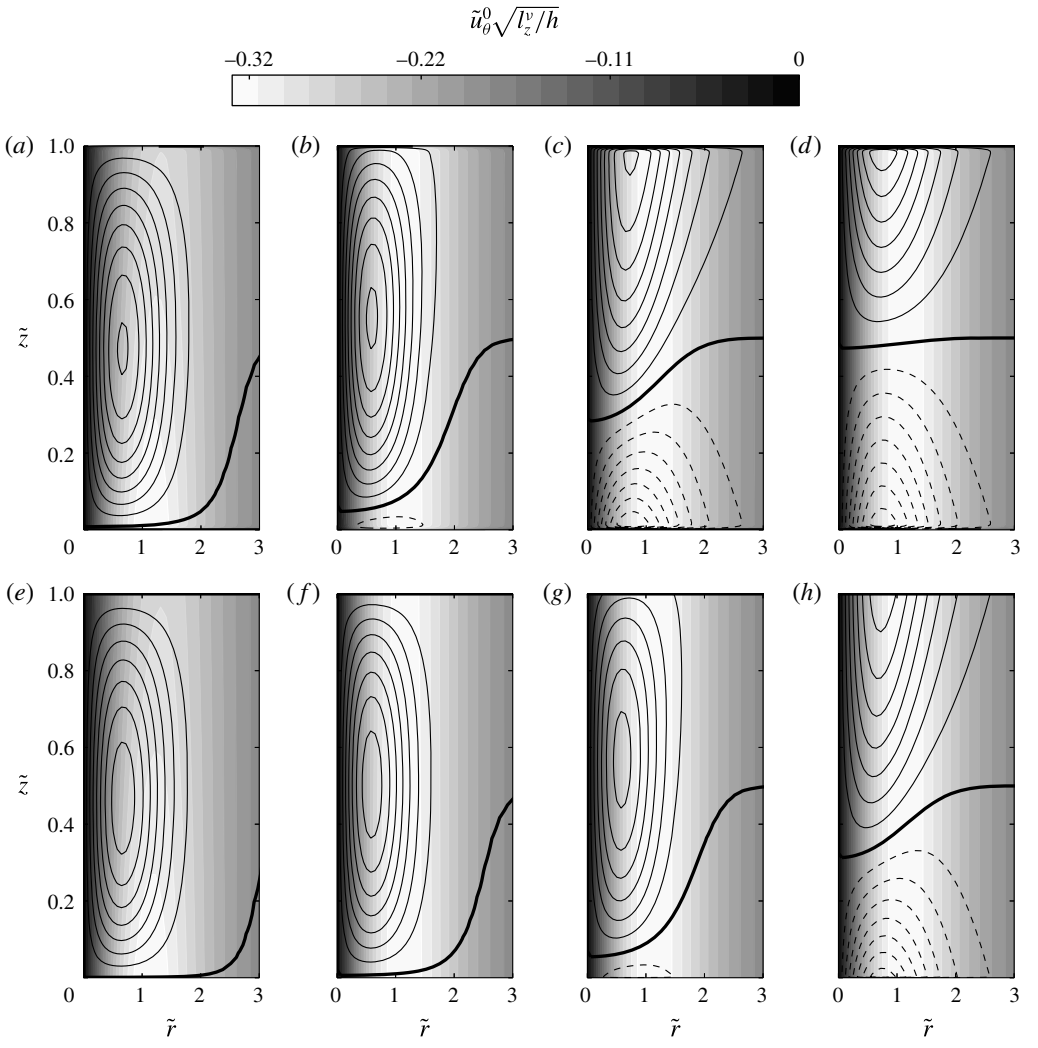

FIGURE 9. Complete velocity field for increasingly quasi-2D base flows. (*a–d*) $Ha = 456$; (*e–h*) $Ha = 3644$. The magnitude of $\tilde{u}_\theta^0$ is indicated by filled contours. Streamlines correspond to iso-values of ψ^1. - - -: clockwise recirculation ($\psi^1 > 0$), ——: counter-clockwise recirculation ($\psi^1 < 0$), ▬: $\psi^1 = 0$. (*a*,*e*) $l_z^v/h = 10$; (*b*,*f*) $= 100$; (*c*,*g*) $= 1000$; (*d*,*h*) $= 10\,000$.

recirculation always exists at the bottom of the channel (though it is not always visible), which results from direct pumping. By contrast, a positive pressure gradient does not exist in the top Hartmann layer for $l_z^v/h = 1$, meaning that in this particular case, the top recirculation is exclusively driven by inverse pumping due to the vertical pressure gradient in the lower half of the channel. As a matter of fact, figure 10 showcases the progressive shift in the mechanism driving the top recirculation, which is not obvious *a priori*, as it does not transpire in its topology. To summarize, direct and inverse pumping co-exist in all cases investigated.

Figure 11 gives a close-up view of the bottom Hartmann layers for the smaller values of l_z^v/h. This figure confirms the existence of a weak clockwise recirculation

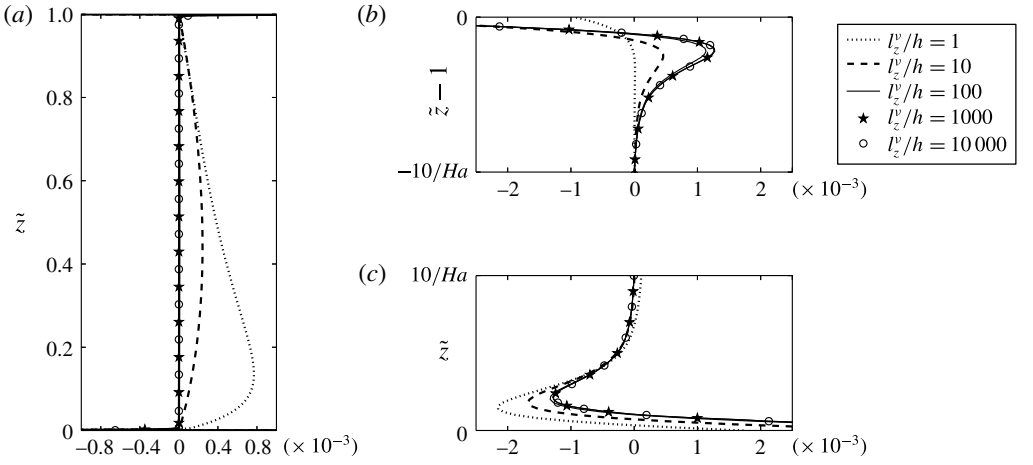

FIGURE 10. Normalized pressure gradient along the axis of the vortex $\partial\tilde{p}^0/\partial\tilde{z}\,(l_z^v/h)^{3/2}$. (*a*) Bulk; (*b*) top Ha layer; (*c*) bottom Ha layer. 3D base flows introduce a positive pressure gradient along $\boldsymbol{e}_z$ in the bulk, which drives a jet to flow down the axis of the channel. In the Hartmann layers, the negative pressure gradient at the bottom pushes the fluid up along the axis, while the positive pressure gradient at the top pulls it down.

in the Hartmann layers, although this direct recirculation is too weak to balance the downwards axial jet. The confinement of this weak direct pumping to the thin boundary layers makes it very difficult to fully capture whether experimentally or numerically. Yet, it is a clear feature of the analytical solution. In addition, figure 11 demonstrates that the Hartmann number does not actually impact the mechanisms driving the meridional flow, but modifies its topology instead by squeezing the streamlines closer to the walls. In order to further quantify the secondary flows, we introduce the poloidal flow rate $q_{\tilde{z}}^1(\tilde{z})$ defined by

$$q_{\tilde{z}}^1(\tilde{z}) = \frac{1}{2}\int_0^{2\pi}\int_0^{\tilde{R}} |\tilde{u}_{\tilde{z}}^1(\tilde{r},\tilde{z})|\,\tilde{r}\,\mathrm{d}\tilde{r}\,\mathrm{d}\theta. \tag{6.2}$$

We also introduce $\tilde{h}_c = h_c/h$, where h_c represents the height of the bottom recirculation. $\tilde{h}_c$ is found as the first local minimum of $q_{\tilde{z}}^1(\tilde{z})$. Figure 12 plots the height of the bottom recirculation against the variable $l_z^v/h\,Ha^{-1}$, which can also be interpreted as the ratio $(\eta/h)^2$ by virtue of (2.2). When the base flow is quasi-2D ($l_z^v/h > 100$), the quantity η/h may naturally be confused with the aspect ratio of the vortex. It appears from figure 12 that when the leading order is close to being quasi-2D, the topology of the meridional flow is fully determined by the parameter η/h. More specifically, narrow aspect ratios correspond to inverse Ekman pumping, while wide aspect ratios lead to an asymptotic state where two counter-rotating structures of equal size split the channel in half. The shift from inverse to direct pumping concurs with a ratio $(\eta/h)^2$ that is of order unity. Note that for a perfectly quasi-2D flow ($l_z^v/h \to \infty$) only direct Ekman pumping subsists for any finite value of η/h.

In order to quantify the relative intensity of secondary flows, we introduce q_{bot} and q_{top}, the mean flow rates occurring inside the bottom and top recirculations,

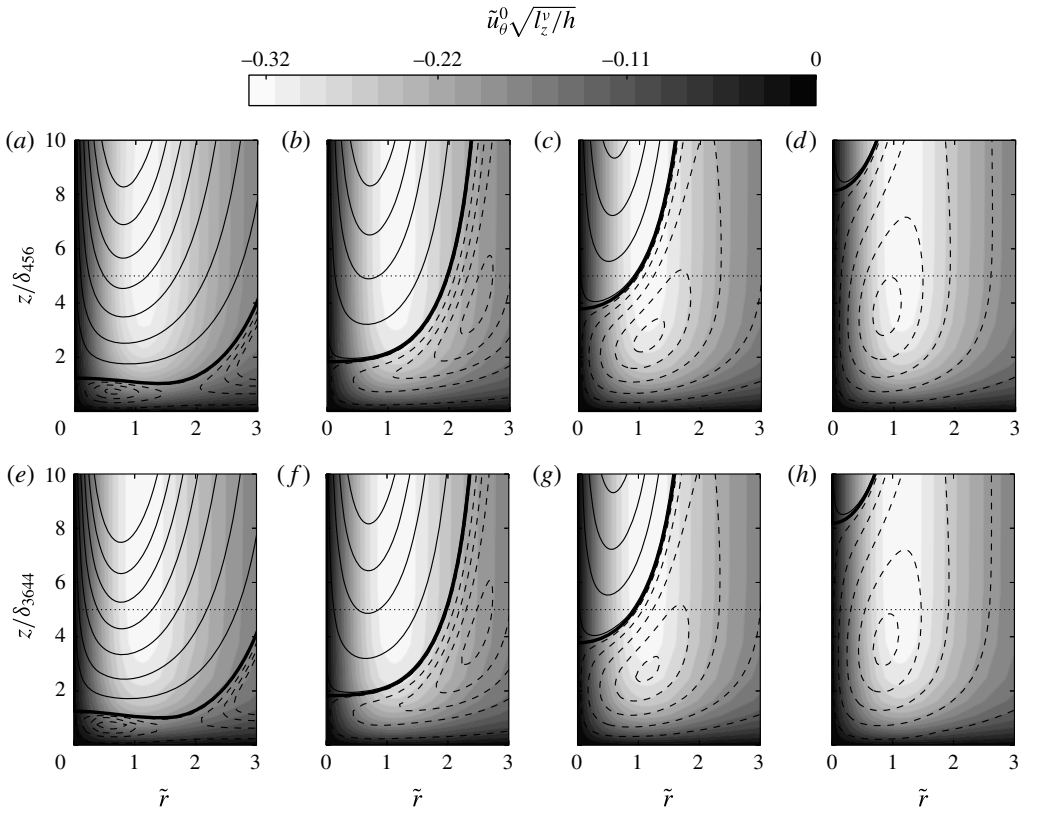

FIGURE 11. Close-up view of the velocity field in the bottom Hartmann layer for 3D base flows. (*a–d*) $Ha = 456$; (*e–h*) $Ha = 3644$. The magnitude of $\tilde{u}_\theta^0$ is indicated by filled contours. Streamlines correspond to iso-values of ψ^1. - - -: clockwise recirculation ($\psi^1 > 0$), ——: counter-clockwise recirculation ($\psi^1 < 0$), ▬: $\psi^1 = 0$. · · · · : plausible positioning of the outer edge of the Hartmann layer located at $z/\delta_{Ha} = 5$, where $\delta_{Ha} = h/Ha$ for $Ha = 456$ and $Ha = 3644$ respectively: (*a*,*e*) $l_z^v/h = 1$; (*b*,*f*) $= 3$; (*c*,*g*) $= 10$; (*d*,*h*) $= 30$.

respectively defined as

$$q_{bot} = \frac{1}{\tilde{h}_c}\int_0^{\tilde{h}_c} q_{\tilde{z}}^1(\tilde{z})\,\mathrm{d}\tilde{z} \quad \text{and} \quad q_{top} = \frac{1}{1-\tilde{h}_c}\int_{\tilde{h}_c}^1 q_{\tilde{z}}^1(\tilde{z})\,\mathrm{d}\tilde{z}. \tag{6.3a,b}$$

According to figure 13, the ratio q_{bot}/q_{top} can also be fully described by the unique variable $(\eta/h)^2$ when the flow is close to being quasi-2D. More specifically, Ekman pumping starts dominating the flow when $(\eta/h)^2$ increases beyond unity, at which point the intensity of both recirculations converges towards the same value.

The behaviours of $\tilde{h}_c$ and q_{bot}/q_{top} are quite similar, which leads to a robust criterion expressing whether the secondary flow is driven by inverse or direct pumping, namely $(\eta/h)^2 > 1$. A phase diagram summarizing all different configurations is reported in figure 14. More specifically, it underlines the fact that inverse pumping can still exist when the base flow is close to being 2D if the vortex is of sufficiently small aspect ratio η/h. This comes from the very nature of direct pumping, which originates within the boundary layers and is therefore strongest there. In thin vortices, its influence on

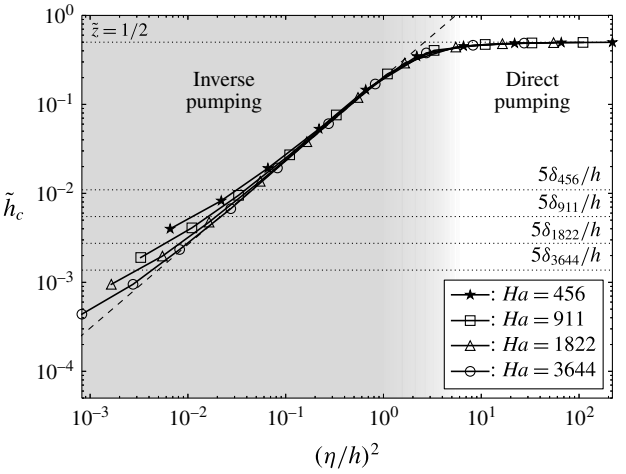

FIGURE 12. Height of the bottom recirculation against $(\eta/h)^2$. The middle of the channel is located at $\tilde{z} = 1/2$. An estimation of the thickness of the bottom Hartmann layer is given by $\tilde{z} = 5\delta_{Ha}/h$, where $\delta_{Ha} = h/Ha$ for $Ha = 456$, 911, 1822 and 3644 respectively.

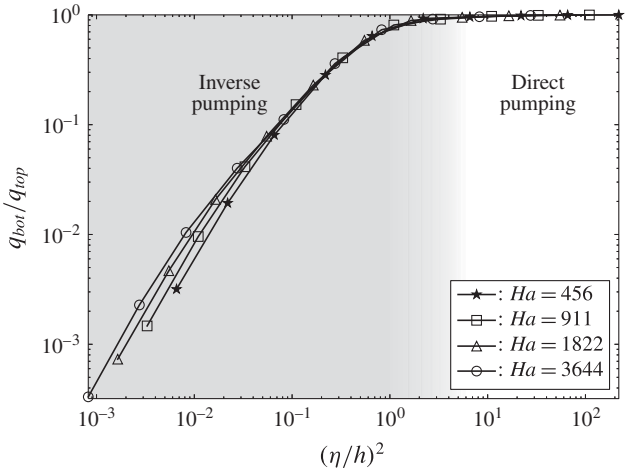

FIGURE 13. Ratio between q_{bot} and q_{top} as a function of $(\eta/h)^2$ for $Ha = 456$, 911, 1822 and 3644.

the bulk is limited, whereas a small pressure gradient in the bulk suffices to drive inverse pumping.

6.3. *Is two-dimensionality a good source of helicity?*

Having now characterized both the azimuthal and meridional flows, we are in a position to determine their potential to generate helicity. Figure 15 displays the helicity $\tilde{H}(\tilde{z})$ integrated over a cross-section of height $\tilde{z}$:

$$\tilde{H}(\tilde{z}) = 2\pi \int_0^{\tilde{R}} \tilde{\boldsymbol{u}} \cdot \tilde{\boldsymbol{\omega}}\, \tilde{r}\, \mathrm{d}\tilde{r}, \tag{6.4}$$

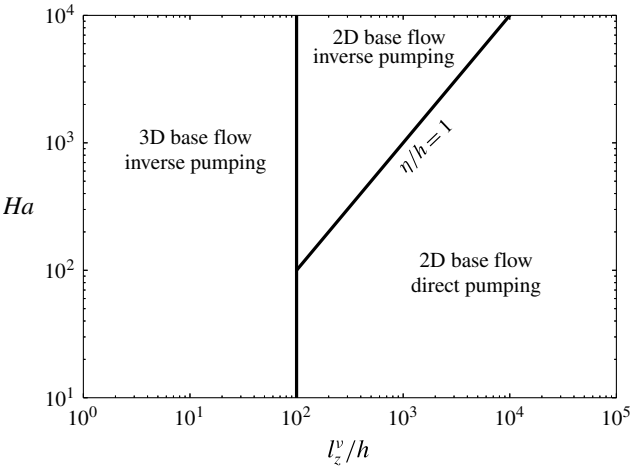

FIGURE 14. Phase diagram summarizing all features of wall-bounded low-*Rm* MHD vortices.

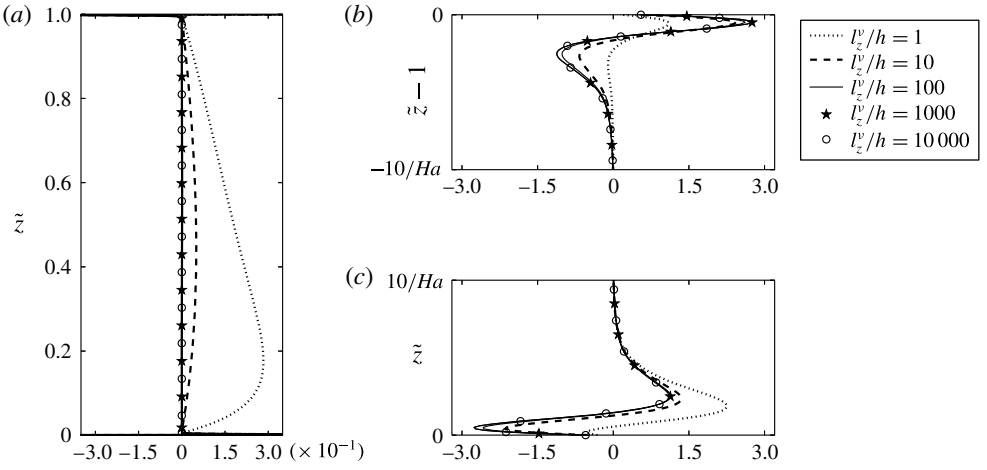

FIGURE 15. Normalized local helicity integrated over horizontal cross-sections $\tilde{H}^1(\tilde{z})(l_z^v/h)$. (*a*) Bulk; (*b*) top Ha layer; (*c*) bottom Ha layer.

which happens to be significant only at first order, i.e. $\tilde{H}(\tilde{z}) = N^{-1}\tilde{H}^1 + O(N^{-3})$, with

$$\tilde{H}^1(\tilde{z}) = 2\pi \int_0^{\tilde{R}} (\tilde{u}_\theta^0\, \tilde{\omega}_\theta^1 + \tilde{u}_{\tilde{r}}^1\, \tilde{\omega}_{\tilde{r}}^0 + \tilde{u}_{\tilde{z}}^1\, \tilde{\omega}_{\tilde{z}}^0)\, \tilde{r}\, \mathrm{d}\tilde{r}. \tag{6.5}$$

Figure 15 suggests that helicity exists in the bulk when the base flow is 3D, while quasi-two-dimensionality confines helicity to the boundary layers. Furthermore, $\tilde{H}^1(\tilde{z})$ is non-symmetrical only for 3D base flows, meaning that the global production of helicity will be non-zero only in this case. Consequently, Ekman pumping does not appear to be the most favourable source of global helicity in MHD vortices, which may seem surprising at first. It can, however, be attributed to several factors. First, secondary flows are a lot stronger when inverse pumping dominates. Second, Ekman

pumping introduces symmetrical structures of opposite sign, which compensate each other globally. Helicity generated by inverse pumping, on the other hand, conserves its sign across the entire layer.

Finally, direct and inverse pumping appear to produce helicity in different ways. While inverse Ekman pumping collocates the axial velocity and vorticity in the bulk, direct pumping produces helicity mainly by combining centripetal jets and shear within the boundary layers.

7. Conclusion

We showed in this paper that the topology of an electrically driven vortex confined between two no-slip walls in the low-*Rm* approximation and weakly inertial limit can be fully described with two parameters. On the one hand, the dimensionality of the leading order is uniquely characterized by the ratio l_z^v/h, which compares the range of action of the Lorentz force to the height of the channel. On the other hand, the topology of the secondary recirculations is fully described by the parameter η/h, which compares the width of the injection electrode to the height of the channel. In the quasi-two-dimensional limit, η/h may be interpreted as the aspect ratio of the vortex.

Thanks to the analytical approach that was undertaken, we were able to completely resolve the finest properties of the flow and in particular the Hartmann boundary layers, which are an inherent source of three-dimensionality. The Hartmann numbers used in this study were comparable to those found experimentally. Using this approach, we were able to distinguish two different inertial mechanisms able to drive the first-order recirculations: inverse and direct Ekman pumping. We found out that both co-existed in all cases investigated (although direct pumping is confined to the bottom boundary layer when the base flow is three-dimensional), and that the shift from one mechanism to the other occurred smoothly. This result could not have been obtained either numerically or experimentally due to a lack of resolution of both approaches at high *Ha*.

Finally, it was found that global helicity is expected to be prominent only in three-dimensional configurations. In a geophysical context, this result might help clarify the question of whether Ekman pumping is a relevant source of helicity to sustain planetary dynamos. As noted by Davidson (2014), Ekman pumping may not be a very efficient source of helicity in planetary cores because quasi-2D vortices extending across the liquid core of the Earth, for example, are unlikely to exist. They can therefore be expected to be three-dimensional, hence favouring alternative mechanisms such as inverse pumping or the propagation of inertial waves.

Acknowledgements

The authors are grateful to the CNRS laboratories LNCMI and CRETA, and in particular to F. Debray and A. Sulpice for hosting and supporting their work. The laboratory SIMAP is part of the LabEx Tec 21 (Investissements d'Avenir – grant agreement no. ANR-11-LABX-0030).

REFERENCES

AKKERMANS, R. A. D., CIESLIK, A. R., KAMP, L. P. J., TRIELING, R. R., CLERCX, H. J. H. & VAN HEIJST, G. J. F. 2008 The three-dimensional structure of an electromagnetically generated dipolar vortex in a shallow fluid layer. *Phys. Fluids* **20**, 116601.

CLERCX, H. J. H. & VAN HEIJST, G. 2009 Two-dimensional Navier–Stokes turbulence in bounded domains. *Appl. Mech. Rev.* **62**, 1–25.

DAVIDSON, P. A. 2014 The dynamics and scaling laws of planetary dynamos driven by inertial waves. *Geophys. J. Intl* **198** (3), 1832–1847.

DAVOUST, L., ACHARD, J.-L. & DRAZEK, L. 2015 Low-to-moderate Reynolds number swirling flow in an annular channel with a rotating end wall. *Phys. Rev.* E **91**, 023019.

DEUSEBIO, E. & LINDBORG, E. 2014 Helicity in the Ekman boundary layer. *J. Fluid Mech.* **755**, 654–671.

EKMAN, V. W. 1905 On the influence of the Earth's rotation on ocean currents. *Ark. Mat. Astron. Fys.* **2**, 1–53.

GILBERT, A. D., FRISCH, U. & POUQUET, A. 1988 Helicity is unnecessary for alpha effect dynamos, but it helps. *Geophys. Astrophys. Fluid Dyn.* **42** (1–2), 151–161.

KALIS, KH. E. & KOLESNIKOV, YU. B. 1980 Numerical study of a single vortex of a viscous incompressible electrically conducting fluid in a homogeneous axial magnetic field. *Magnetohydrodynamics* **16**, 155–158.

KLEIN, R. & POTHÉRAT, A. 2010 Appearance of three-dimensionality in wall bounded MHD flows. *Phys. Rev. Lett.* **104** (3), 034502.

KORNET, K. & POTHÉRAT, A. 2015 A method for spectral DNS of low *Rm* channel flows based on the least dissipative modes. *J. Comput. Phys.* **298**, 266–279.

LINDBORG, E. 1999 Can the atmospheric kinetic energy spectrum be explained by two-dimensional turbulence? *J. Fluid Mech.* **388**, 259–288.

MESSADEK, K. & MOREAU, R. 2002 An experimental investigation of MHD quasi-two-dimensional turbulent shear flows. *J. Fluid Mech.* **456**, 137–159.

POTHÉRAT, A. & KLEIN, R. 2014 Why, how and when MHD turbulence at low *Rm* becomes three-dimensional. *J. Fluid Mech.* **761**, 168–205.

POTHÉRAT, A., RUBICONI, F., CHARLES, Y. & DOUSSET, V. 2013 Direct and inverse pumping in flows with homogeneous and non-homogeneous swirl. *Eur. Phys. J.* E **36** (8), 94.

POTHÉRAT, A., SOMMERIA, J. & MOREAU, R. 2000 An effective two-dimensional model for MHD flows with transverse magnetic field. *J. Fluid Mech.* **424**, 75–100.

POTHÉRAT, A., SOMMERIA, J. & MOREAU, R. 2002 Effective boundary conditions for magnetohydrodynamic flows with thin Hartmann layers. *Phys. Fluids* **14** (1), 403–410.

ROBERTS, P. H. 1967 *Introduction to Magnetohydrodynamics*. Longmans.

SATIJN, M. P., CENSE, A. W., VERZICCO, H., CLERCX, H. J. H. & VAN HEIJST, G. J. F. 2001 Three-dimensional structure and decay properties of vortices in shallow fluid layers. *Phys. Fluids* **13** (7), 1932–1945.

SHATS, M., BYRNE, D. & XIA, H. 2010 Turbulence decay rate as a measure of flow dimensionality. *Phys. Rev. Lett.* **105**, 264501.

SMITH, D. M. 1991 Algorithm 693: a Fortran package for floating-point multiple-precision arithmetic. *ACM Trans. Math. Softw.* **17** (2), 273–283.

SOMMERIA, J. 1988 Electrically driven vortices in a strong magnetic field. *J. Fluid Mech.* **189**, 553–569.

SOMMERIA, J. & MOREAU, R. 1982 Why, how and when MHD turbulence becomes two-dimensional. *J. Fluid Mech.* **118**, 507–518.

TABELING, P. 2002 Two-dimensional turbulence: a physicist approach. *Phys. Rep.* **362** (1), 1–62.